RSC Advances

PAPER

View Article Online
View Journal | View Issue

Cite this: *RSC Adv.*, 2017, **7**, 9130

First-principles investigation of the surface properties of fergusonite-type monoclinic $BiVO_4$ photocatalyst

Guo-Ling Li*

Fergusonite-type monoclinic $BiVO_4$ (fm-$BiVO_4$) is an important semiconductor photocatalyst as an alternative to TiO_2 for solar energy conversion and environmental protection. Based upon density functional theory (DFT) calculations, we report the results of a comprehensive study of the surface properties of fm-$BiVO_4$, including surface geometric/electronic structures, surface energy, work function, Bader charge, and oxygen-vacancy formation energy on the (100), (010), (001), (101), (011), (110) and (111) surfaces. The low-index surfaces of fm-$BiVO_4$ are characterized by surface geometric structures terminated with Bi atoms and VO_4 groups. There are strongly localized band-gap states at the (110) and (111) surfaces. The calculated surface energies of fm-$BiVO_4$ indicate a surface stability order of {001} > {011} ~ {101} > {111} > {110} > {010} ~ {100}. The equilibrium morphology of fm-$BiVO_4$ is predicted as a corner-cut truncated bipyramid with {001}, {101}, {011} and {111} facets exposed, in good agreement with experiments. The dramatic difference in work function may act as the driving force for photogenerated charge separation between {101}/{011} and {001} as observed in experiments. Based on our results, we provide a clue to morphology design for further enhancing the efficiency of charge separation in fm-$BiVO_4$.

Received 10th December 2016
Accepted 18th January 2017

DOI: 10.1039/c6ra28006d

rsc.li/rsc-advances

1 Introduction

The surface physicochemical properties of semiconductor oxides are crucial in applications such as heterogeneous catalysis, molecule adsorption, gas sensing, and energy conversion and storage.[1] To improve the desired physicochemical properties, semiconductor facets can be fine-tuned *via* morphology control strategies. For example, the {001} facets of anatase TiO_2 are known to be especially reactive for photocatalysis. However, the {001} facets are the minority among exposed facets in the equilibrium morphology of anatase. It is desirable to synthesize anatase single crystals with a high percentage of {001} facets in order to improve the photocatalytic activity. Such a strategy has been successfully demonstrated recently.[2] The success in morphology control for anatase depends on the knowledge of the surface physics and chemistry of TiO_2 that have been extensively studied.[3]

Much attention has been paid to bismuth vanadate $BiVO_4$ due to its novel properties such as ferroelasticity,[4] ionic conductivity,[5] and acousto-optical[6] and photochromic[7] effects. With a high chemical stability, $BiVO_4$ could be used as a nontoxic yellow pigment,[8] potential cathode material in lithium cells,[9] promising gas sensor,[10] and good catalyst for the selective oxidation of olefins[11] and H_2S.[12] Especially, under visible light irradiation, $BiVO_4$ can robustly evolve O_2 from water in the presence of sacrificial reagents (*e.g.*, Ag^+ and Fe^{3+} ions),[13] selectively reduce CO_2 into ethanol,[14] photochemically decompose organic pollutants and oxidize inorganic chemicals such as NO,[15] synthesize H_2O_2 from water and O_2,[16] and act as an efficient photoanode in photoelectrochemical cells.[17,18] In this sense $BiVO_4$ is considered as an important alternative photocatalyst to TiO_2 for solar energy conversion and environmental protection.[19]

$BiVO_4$ comprises four polymorphs, *i.e.*, pucherite, dreyerite, clinobisvanite, and scheelite-type tetragonal phase.[4,20] Among them clinobisvanite, *i.e.*, fergusonite-type monoclinic $BiVO_4$ (fm-$BiVO_4$), is stable at ambient temperature and pressure, and is most often used as a photocatalyst. It has been found that the morphology of fm-$BiVO_4$ has a strong impact on the photocatalytic activity, and much effort has been devoted to the controllable synthesis of fm-$BiVO_4$ with specific morphologies.[10,21–24] In particular, it has been confirmed that the photogenerated electrons and holes can be efficiently separated between different crystal facets of fm-$BiVO_4$.[25]

To reveal the underlying structure–property relationships, density functional theory (DFT) calculations have been carried out for $BiVO_4$, mainly for fm-$BiVO_4$.[18,22,26–35] Emphasis is placed on the role of Bi 6s orbitals which contain stereoactive electron lone pairs.[26–29] For example, based on the calculated density of states (DOS), the Bi 6s orbitals are found to contribute considerably to the valence band (VB) top, and are inferred to result in

School of Physics and Engineering, Henan University of Science and Technology, Luoyang 471023, China. E-mail: guoling.li@gmail.com; liguoling@dicp.ac.cn

a large hole mobility as well as the excellent photocatalytic activity of fm-$BiVO_4$.[26] Walsh *et al.* concluded that fm-$BiVO_4$ is a direct bandgap semiconductor.[28,29] However, Zhao *et al.* calculated fm-$BiVO_4$ as an indirect one.[30,31] The optical functions of fm-$BiVO_4$ were calculated,[28,30] and the strong optical anisotropy was related to the morphology dependence of photocatalytic activity.[30] Doping properties were well studied for fm-$BiVO_4$, based on which the doping impact on the photocatalytic or photoelectrochemical properties was discussed.[31–34,36] Zhao *et al.* also calculated the surface energies of fm-$BiVO_4$.[37] The water adsorption properties on the (100) surface of fm-$BiVO_4$ were investigated by a first-principles molecular dynamics approach, indicating that water is adsorbed molecularly at the fivefold-coordinated Bi site where water oxidization is supposed to occur.[35]

Compared to TiO_2, $BiVO_4$ is a much less studied semiconductor oxide, especially with respect to its surface properties. Here we report the comprehensive results of first-principles calculations of surface properties for fm-$BiVO_4$. Low-index surfaces, *i.e.*, (100), (010), (001), (101), (011), (110) and (111), are considered. Structural effects are carefully taken into account to understand the calculated surface properties including surface geometric/electronic structures, surface energy, work function, Bader charge, and oxygen-vacancy formation energy. The predicted equilibrium morphology of fm-$BiVO_4$ is compared with the experimental one. We also discuss the possible driving force for photogenerated charge separation in photocatalysis, and provide clues to morphology design for further enhancing the efficiency of charge separation in fm-$BiVO_4$.

2 Crystal structure and computational methodology

The crystal structure of fm-$BiVO_4$ belongs to point group C_{2h}^6 and space group no. 15 in the international tables for crystallography. As is known, space group no. 15 has one conventional setting $C2/c$ and several nonconventional settings such as $I2/a$, $I2/b$ and $B2/b$. For fm-$BiVO_4$, experimentalists were used to the body-centered setting $I2/a$ while theorists preferred the base-centered setting $C2/c$.[28,30,31,34,36,37] However, it is better to take the body-centered setting $I2/b$ for fm-$BiVO_4$ in order to make a direct comparison between the body-centered monoclinic fm-$BiVO_4$ and the body-centered tetragonal $BiVO_4$.[4,5,33] In this work, we take the setting $I2/b$ for the bulk and surfaces of fm-$BiVO_4$. For the sake of convenience, we present in Table 1 the corresponding low indices of crystal face in the representation of the settings $I2/a$, $B2/b$ and $C2/c$ according to transformation matrices between these settings.[38]

Fig. 1 shows the crystal structure of fm-$BiVO_4$, a body-centered monoclinic cell in the setting $I2/b$.[4,20] In view of centrosymmetry, we can classify fm-$BiVO_4$ as a non-polar oxide. Owing to the weak symmetry breaking in the *a*–*b* plane, the crystal structure of fm-$BiVO_4$ can be taken as a slight distortion of the scheelite-type tetragonal structure. Due to the distortion, there are two kinds of inequivalent oxygens, *i.e.*, O(1) and O(2), both coordinated to two Bi atoms and one V atom. The isolated VO_4 tetrahedron with the V atom surrounded by four oxygen atoms in a distorted tetrahedral geometry is coordinated to eight neighboring Bi atoms. The Bi atom together with the BiO_8 dodecahedron is surrounded by eight VO_4 tetrahedra. In addition, the BiO_8 dodecahedron shares four edges with neighboring BiO_8 dodecahedra but no edges with any VO_4 tetrahedra. According to crystal chemistry, the structure of fm-$BiVO_4$ can be regarded as made up of Bi^{3+} cations and VO_4^{3-} anions. Table 2 lists the measured structural parameters.[20]

DFT calculations are done using the projector-augmented wave method[39] and a plane-wave basis set as implemented in the Vienna Ab Initio Simulation Package (VASP).[40] The generalized gradient approximation (GGA) formulated by Perdew, Burke and Ernzerhof (PBE) is taken for the exchange–correlation functional.[41] The valence configurations are treated as $6s^2$ $6p^3$ for Bi, $3d^3$ $4s^2$ for V, and $2s^2$ $2p^4$ for O. The cutoff energy for plane-wave basis functions is 400 eV. For simplification, the γ angle of fm-$BiVO_4$ is approximated to 90°,[26,28] which removes the tiny differences between $\{11k\}$ and $\{1\bar{1}k\}$ surfaces ($k = 0, 1$). For bulk structure optimization, calculations are done in a $10 \times 10 \times 6$ Monkhorst–Pack (MP) *k*-point mesh with lattice parameters *a*, *b*, *c* varied and internal parameters (*x*, *y*, *z*) relaxed, based on which a $5 \times 5 \times 5$ three-dimensional energy

Table 1 Low indices of crystal face in the setting $I2/b$ for fm-$BiVO_4$ and the corresponding ones in the settings $I2/a$, $B2/b$ and $C2/c$, respectively

Settings	Low indices of crystal face						
$I2/b$	{100}	{010}	{001}	{101}	{011}	{110}	{111}
$I2/a$	{001}	{100}	{010}	{011}	{110}	$\{10\bar{1}\}$	$\{11\bar{1}\}$
$B2/b$	{100}	$\{\bar{1}10\}$	{001}	{101}	$\{1\bar{1}1\}$	{010}	$\{01\bar{1}\}$
$C2/c$	{100}	$\{\bar{1}01\}$	{010}	$\{\bar{1}10\}$	$\{\bar{1}11\}$	{001}	{011}

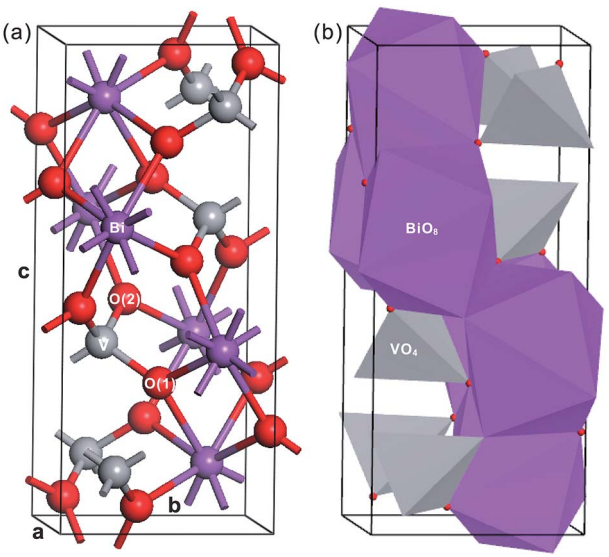

Fig. 1 Crystal structure of fm-$BiVO_4$. (a) In the ball-stick model and (b) in the polyhedron model. The Bi, Ti and O atoms are in purple, gray and red, respectively.

Table 2 Comparison of the experimental and calculated structural parameters of bulk fm-$BiVO_4$ in the setting *I*2/*b*. The Wyckoff positions are at (*x*, *y*, *z*)

		Exp. (295 K)[20]			Cal. (GGA-PBE)		
a (Å)		5.1935			5.177		
b (Å)		5.0898			5.145		
c (Å)		11.6972			11.769		
γ (°)		90.3870			90		
	Wyckoff	*x*	*y*	*z*	*x*	*y*	*z*
Bi	4(e)	0.0000	0.2500	0.6335	0.000	0.250	0.626
V	4(e)	0.0000	0.2500	0.1300	0.000	0.250	0.127
O(1)	8(f)	0.1465	0.5077	0.2082	0.142	0.502	0.205
O(2)	8(f)	0.2606	0.3810	0.4493	0.251	0.388	0.452

grid is obtained. The equilibrium structural parameters are derived from the lowest energy point on the interpolated energy grid. The non-polar (100), (010), (001), (101), (011), (110) and (111) surface slabs with 6, 7, 8, 9 and 10 layers of Bi/V cations are generated from the optimized bulk lattice. A 12 Å vacuum layer is added in the crystallographic planes of interest. We use a 4 × 2 × 1 MP *k*-point mesh for the (100) and (111) surfaces, 2 × 4 × 1 for the (010) surface, 4 × 4 × 1 for the (110) surface, and 4 × 6 × 1 for the (101) and (011) surfaces. For each surface slab, we use a conjugate-gradient algorithm to relax the atomic positions until forces converge to less than 0.02 eV $Å^{-1}$ prior to the total energy calculation. It should be noted that the surface slabs with 8 layers of cations are thick enough for calculating surface electronic structures, Bader charges, work functions, and O-vacancy formation energies. The surface slabs with 6, 7, 8, 9 and 10 layers of cations are used to obtain accurate surface energies which are crucial to morphology prediction for fm-$BiVO_4$. For slab calculations, dipole correction is taken into account. All the calculations are non-spin-polarized except those for O-vacancy formation energies.

3 Computational results

3.1 Bulk geometric and electronic structures

The optimized structural parameters of fm-$BiVO_4$ are presented in Table 2, in good agreement with the experiment.[20] In the same representation of space group, our optimized lattice constants *a*, *b* and *c* are quite close to those calculated by Walsh *et al.*[28] The V–O bond lengths d_{V-O} are calculated to be 1.739 and 1.751 Å, and the Bi–O bond lengths d_{Bi-O} are 2.432, 2.451, 2.473 and 2.532 Å.

Fig. 2 shows the site-projected partial DOS and chemical bonding analysis of fm-$BiVO_4$ in the energy range from −20 eV to 5 eV. Here, Crystal Orbital Overlap Population (COOP) for chemical bonding analysis is done with the computer program LOBSTER,[42] based on the PAW results calculated using VASP. The Bi 6s states are located predominantly around −9.3 eV, and partially around −17 eV and between −2.5 to 0 eV. However, the Bi–O bonding magnitude is rather small around −9.3 eV compared to those around −17 eV and between −2.5 to 0 eV.

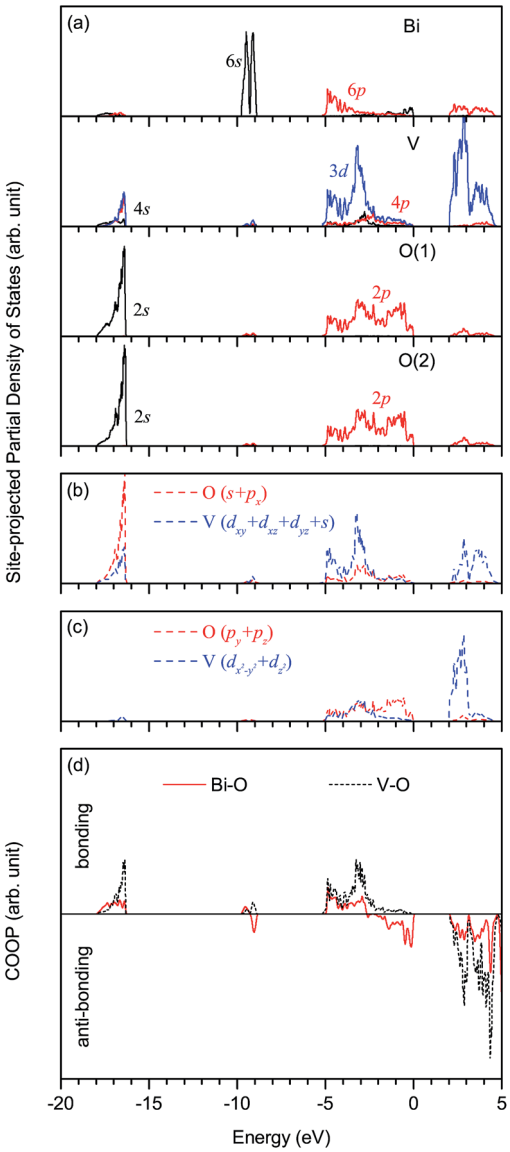

Fig. 2 Site-projected partial density of states of fm-$BiVO_4$: (a) for s, p and d orbitals of Bi, V, O(1) and O(2) atoms, (b) for V (d_{xy} + d_{xz} + d_{yz} + s) and O (s + p_x) hybrid orbitals, and (c) for V (d_{z^2} + $d_{x^2-y^2}$) and O (p_y + p_z) orbitals. (d) COOP curves for the Bi–O and V–O bonds. The Fermi level is at zero energy.

Thus, the Bi 6s orbital can be characterized as strongly non-bonding around −9.3 eV, weakly bonding around −17 eV and anti-bonding between −2.5 to 0 eV. There are notable Bi 6p states below the Fermi level, indicating that the Bi atom is not fully ionized into the expected Bi^{3+} cation. The mixing between the Bi 6p orbital and the O 2p orbital occurs mainly around −5 to −3 eV (bonding) and above 2 eV (anti-bonding). As in CrO_4^{2-} and MnO_4^{-},[43] the d^3s ($3d_{xy}$, $3d_{xz}$, $3d_{yz}$, 4s) hybrid orbitals of vanadium in VO_4^{3-} dominate in the tetrahedral hybridization with considerable mixing among the V 3d and 4p orbitals. The inequivalent O(1) and O(2) have an overall similar DOS with the 2s orbital around −17 eV and the 2p orbital around the Fermi level. As shown in Fig. 2(b), the V d^3s hybrid orbitals overlap with the O sp (2s, $2p_x$) hybrid orbitals, forming four σ bonds. In

Fig. 2(c), the empty V $3d_{x^2-y^2}$ and $3d_{z^2}$ orbitals overlap with the O $2p_y$ and $2p_z$ orbitals, resulting in two delocalized 5-center-8-electron Π_5^8 bonds.[43] The main charge compositions are the O 2p (64.7%) and Bi 6s (12.6%) states at the VB edge, and the V 3d (70.7%) and Bi 6p (11.7%) states at the conduction band (CB) edge. In particular, the O $2p_y$ and $2p_z$ orbitals contribute 51.0% at the VB edge, and the V $3d_{x^2-y^2}$ and $3d_{z^2}$ orbitals 67.0% at the CB edge, implying that the Π_5^8 bonds play the most important role in physical properties determined by band edges. The calculated band gap E_g is 2.07 eV, close to the reported values.[26,28,30–34]

3.2 Surface cleavage

The surface cleavage of fm-$BiVO_4$ involves Bi–O and/or V–O bond disruption. It has been noted that the V–O bond strength in the rigid VO_4 tetrahedron is much stronger than the Bi–O bond strength in the BiO_8 dodecahedron.[44] Thus, the surface of fm-$BiVO_4$ is likely to consist of Bi cations and VO_4 tetrahedra on all faces.[11]

Here we make an estimate of the Bi–O and V–O bond energies. Considering the (100) surface unit cell, there are 12 Bi–O bonds disrupted in the expected termination with Bi–O–V and VO_4 groups at the surface.[11,26] In another possible termination with Bi–O–Bi and VO_3 groups at the surface, there are only 6 Bi–O and 2 V–O bonds disrupted. The latter termination is 1.96 eV higher in energy than the former one for each surface Bi or V atom. Assuming simply that all Bi–O (V–O) bonds are identical, we obtain the Bi–O (V–O) bond energy E_{Bi-O} (E_{V-O}) in terms of $(E_{slab}^{unrel} - E_{bulk})/2 = N_{Bi-O}E_{Bi-O} + N_{V-O}E_{V-O}$, where E_{slab}^{unrel} denotes the total energy of the unrelaxed slab, E_{bulk} is the corresponding total energy of the bulk, and N_{Bi-O} (N_{V-O}) is the number of disrupted Bi–O (V–O) bonds at the surface. E_{Bi-O} is then estimated to be 0.52 eV and E_{V-O} is estimated as 3.54 eV, indicating that the Bi–O bond strength is much weaker than the V–O bond strength.

Thus, we make sure that the stable surfaces of fm-$BiVO_4$ are terminated with Bi atoms and VO_4 groups, directly supporting the above-mentioned argument from crystal chemistry.[11,44]

3.3 Surface geometric and electronic structures

Based on the optimized structural parameters, we constructed the surface slabs of fm-$BiVO_4$. It should be noted that, due to the weak symmetry breaking in the *a*–*b* plane, there are only trivial differences between {100} and {010} in the surface geometric structures of fm-$BiVO_4$. It is the same between {101} and {011}. According to the structure–property relationships, physical properties, *e.g.*, surface electronic structures, surface energies and work functions, are expected to be similar for {100}/{010} or {101}/{011}.

3.3.1 The {100}/{010} surfaces. The relaxed geometric structure of the fm-$BiVO_4$ (100) surface is shown in Fig. 3(a) and (b). The fivefold-coordinated surface Bi atoms exhibit a characteristic zigzag chain along the [010] direction. The adjacent Bi^{3+} cations on the chain are not effectively screened from each other. The nearest neighboring Bi atoms with a distance of 4.40 Å provide possible bridge sites for adsorption of anions or molecules. The surface VO_4 group, containing onefold-coordinated O1′ and twofold-coordinated O1, also forms a zigzag chain along the [010] direction. The O1′ atom has an apparent V=O double bond with a bond length of 1.614 Å, as presented in Table 3. The surface V–O bond length is 1.755 Å, close to the bulk values. In the unrelaxed slab of fm-$BiVO_4$ (100), the surface Bi and V atoms are coplanar in the surface plane. In the relaxed slab, the surface Bi atom moves inward 0.13 Å while the surface V atom moves outward 0.07 Å along the [100] direction.

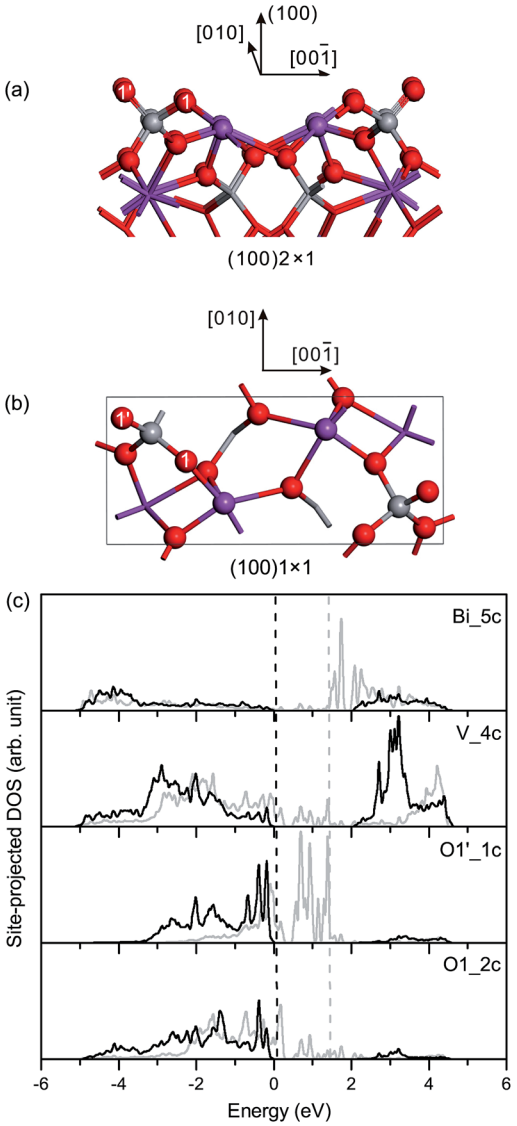

Fig. 3 (a) Side view and (b) top view of the relaxed geometric structure of the fm-$BiVO_4$ (100) surface. For clarification, atoms underneath surface BiO_5 and VO_4 polyhedra are given in the stick model. (c) Site-projected DOS of specific surface atoms in the relaxed and unrelaxed (100) surface slabs, denoted by black and grey, respectively. The label Bi_5c represents the fivefold-coordinated surface Bi atom, and it is similar for surface V, O1′ and O1 atoms. The dashed vertical lines represent the Fermi levels. The VB and CB edges of bulk fm-$BiVO_4$, determined from the site-projected DOS of interior-most atoms, are at 0 eV and 2.07 eV, respectively.

Table 3 Bond lengths d_{V-O} and $d_{V=O}$ in Å in the bulk and on the surfaces of fm-$BiVO_4$

	Bulk	(100)	(010)	(001)	(101)	(011)	(110)	(111)
d_{V-O}	1.739	1.755	1.756	1.692	1.686	1.688	1.730	1.727
	1.751				1.718	1.718	1.667	1.679
					1.707	1.704		1.733
								1.670
$d_{V=O}$		1.614	1.614				1.629	1.630
								1.620

Fig. 3(c) shows the site-projected DOS of specific surface atoms in the relaxed and unrelaxed (100) surface slabs, denoted by black and grey curves, respectively. For the unrelaxed slab, the empty backbond 6p states of the surface Bi atom lie in the bulk band-gap region. The Π_5^8 bonds are totally broken in the surface VO_4 group. The occupied backbond 2p states of the surface O1′, overlapping heavily with the V 3d states, are located in the bulk band-gap region too. As is known, surface relaxation often shifts the occupied ideal surface states down and the empty ideal surface states up in energy.[45] Thus, for the relaxed slab, surface relaxation makes the band-gap surface states merge into the bulk region. Only O 2p-derived resonances are found in the upper valence band region, and the surface Fermi level almost coincides with the bulk one.

3.3.2 The {001} surface. Fig. 4(a) and (b) show the relaxed geometric structure of the fm-$BiVO_4$ (001) surface. The surface Bi atoms are sixfold coordinated, and the surface O atoms twofold coordinated. The surface V–O bond length is 1.692 Å, slightly shorter than the bulk values. The surface Bi^{3+} cations are well screened by neighboring VO_4^{3-} anions, and *vice versa*. In the unrelaxed slab of fm-$BiVO_4$ (001), the surface Bi and V atoms are coplanar in the surface plane. In the relaxed slab, the surface Bi and V atoms move inwards along the [001] direction by 0.11 Å and 0.03 Å, respectively.

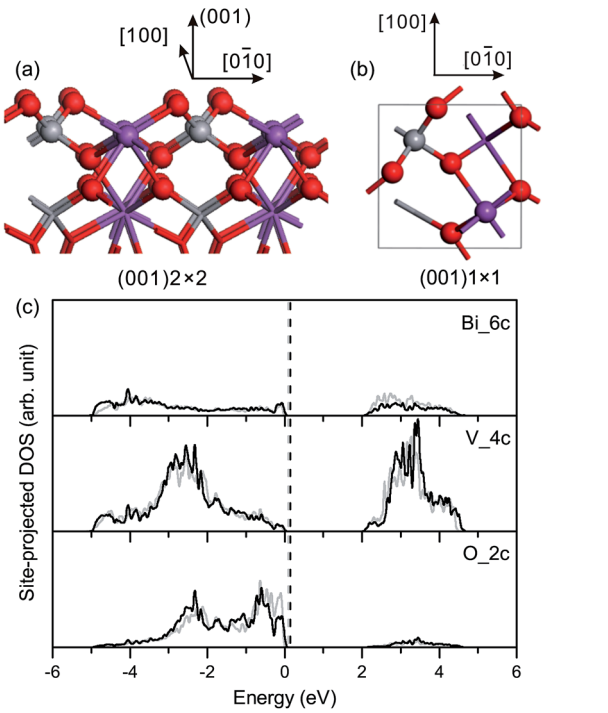

Fig. 4 (a) Side view and (b) top view of the relaxed geometric structure of the fm-$BiVO_4$ (001) surface. (c) Site-projected DOS of specific surface atoms in the relaxed and unrelaxed (001) surface slabs, denoted by black and grey, respectively.

Surface relaxation is negligible for the fm-$BiVO_4$ (001) surface, and the site-projected DOS of specific surface atoms is similar for the relaxed and unrelaxed surface slabs, as shown in Fig. 4(c). The Π_5^8 bonds remain in the surface VO_4 group with an increase in the bonding–antibonding splitting. No band-gap states occur in the band-gap region.

3.3.3 The {101}/{011} surfaces. Fig. 5(a) and (b) show the relaxed geometric structure of the fm-$BiVO_4$ (101) surface. The surface Bi atom is fivefold coordinated. The surface and subsurface VO_4 groups have twofold-coordinated O1, O2, and O3 atoms, respectively. The surface V–O bond lengths are shorter than the bulk values, as given in Table 3. In the unrelaxed slab of fm-$BiVO_4$ (101), the outermost layer is the surface Bi atom, the sublayer the surface VO_4 group, and the subsublayer the subsurface VO_4 group. Thus, the surface Bi atoms are not screened from each other. In the relaxed slab, the surface Bi atom moves inward 0.25 Å, the surface V atom outward 0.11 Å, and the subsurface V atom inward 0.04 Å.

Fig. 5(c) shows the site-projected DOS of specific surface atoms in the relaxed and unrelaxed (101) surface slabs. For the unrelaxed slab, the empty backbond 6p states of the surface Bi atom are located in the bulk band-gap region. The Π_5^8 bonds remain in the surface and subsurface VO_4 groups, with an increase in the bonding-antibonding splitting. For the relaxed slab, the surface states of Bi 6p disappear due to surface relaxation, and no band-gap states occur in the band-gap region.

3.3.4 The {110} surface. Fig. 6(a) and (b) show the relaxed geometric structure of the fm-$BiVO_4$ (110) surface. The coordination number is five for the surface Bi1 atom, and seven for the subsurface Bi2 atom. The bridge site between Bi1 and Bi2 is possibly responsible for adsorption of anions or molecules. In the surface VO_4, O1′ is onefold coordinated and O1 twofold coordinated. In the subsurface VO_4, O2 is twofold coordinated. The surface Bi atoms (or VO_4 groups) are well screened from each other. The bond length of V=O is 1.629 Å at the (110) surface, slightly longer than that at the (100)/(010) surface. In the unrelaxed slab, the Bi1 (Bi2) and V1 (V2) atoms are coplanar in the surface plane. In the relaxed slab, Bi1, Bi2 and V1 atoms move inward 0.15 Å, 0.04 Å and 0.02 Å, respectively, and the V2 atom moves outward 0.04 Å along the [100] direction.

Fig. 6(c) shows the site-projected DOS of specific surface atoms in the relaxed and unrelaxed (110) surface slabs. The Π_5^8 bonds remain in the surface and subsurface VO_4 groups. The bonding–antibonding splitting of Π_5^8 is larger in the surface VO_4 than in the subsurface VO_4. For the unrelaxed slab, two sharp peaks of occupied dangling-bond states lie in the band-gap region. The two dangling bonds are derived from the Π_5^8 bonds in the surface VO_4. Due to surface relaxation, one peak of the dangling-bond states merges into the bulk VB region, and the other is fixed at 0.1–0.2 eV above the VB top.

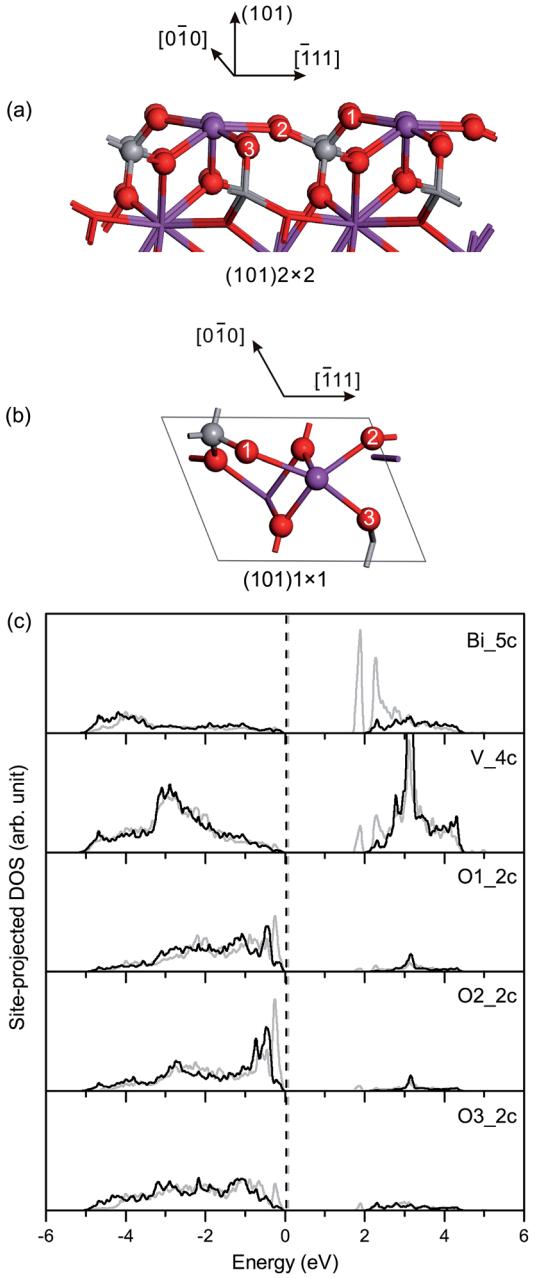

Fig. 5 (a) Side view and (b) top view of the relaxed geometric structure of the fm-$BiVO_4$ (101) surface. (c) Site-projected DOS of specific surface atoms in the relaxed and unrelaxed (101) surface slabs, denoted by black and grey, respectively.

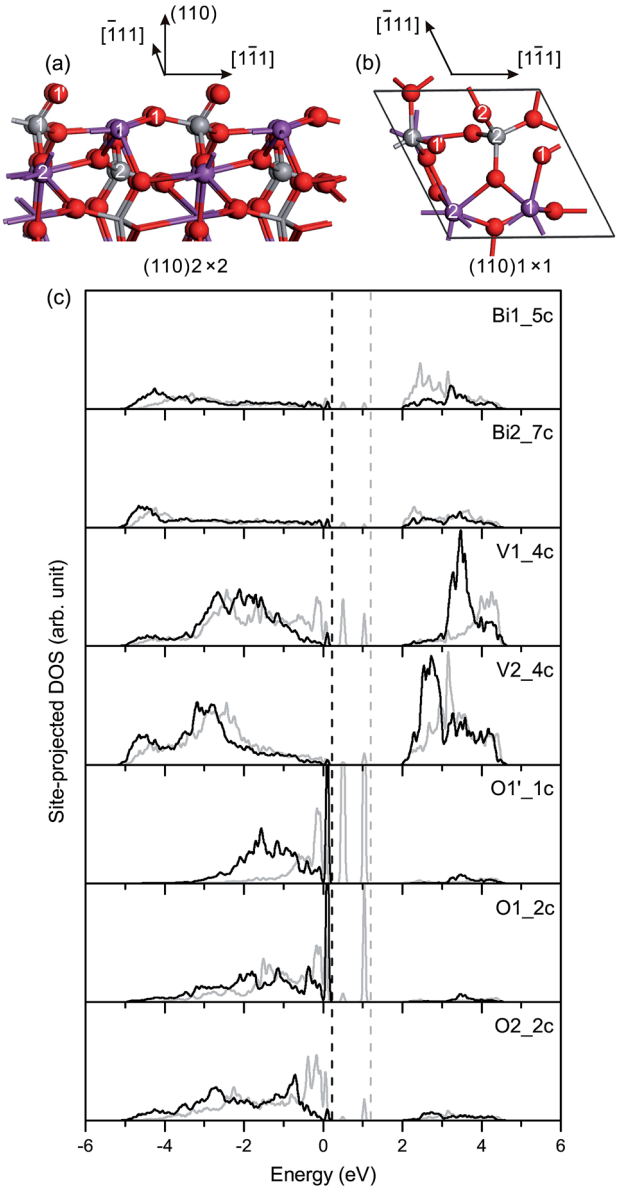

Fig. 6 (a) Side view and (b) top view of the relaxed geometric structure of the fm-$BiVO_4$ (110) surface. (c) Site-projected DOS of specific surface atoms in the relaxed and unrelaxed (110) surface slabs, denoted by black and grey, respectively.

Thus, there are dangling-bond states in the band-gap region of the (110) surface.

3.3.5 The {111} surface. Fig. 7(a) and (b) show the relaxed geometric structure of the fm-$BiVO_4$ (111) surface. The (111) surface consists of terraces separated by steps. Bi2 and Bi3 on the terrace are both sixfold coordinated, and Bi1 and Bi4 on the step are fivefold and sevenfold coordinated, respectively. There are two bridge sites for adsorption of anions or molecules, one between Bi2 and Bi3 and the other between Bi1 and Bi4. In the $V1O_4$ group, O1′ is onefold coordinated and O1 twofold coordinated. In the $V2O_4$ group, O2′ is onefold coordinated. In the $V3O_4$ group, both O2 and O3 are twofold coordinated. In the $V4O_4$ group, O4 is twofold coordinated. The surface Bi atoms (VO_4 groups) are well screened from each other. The bond length of V=O on the (111) surface is nearly the same as that on the (110) surface, as given in Table 3. In the unrelaxed slab, the Bi and V atoms are coplanar in the surface plane. In the relaxed slab, Bi1, Bi2, Bi3 and Bi4 atoms move inward 0.11 Å, 0.13 Å, 0.04 Å and 0.07 Å, respectively. However, the four surface V atoms do not move much along the [100] direction (≤0.01 Å).

Fig. 7(c) shows the site-projected DOS of specific surface atoms in the relaxed and unrelaxed (111) surface slabs. The Π_5^8 bonds remain in the surface VO_4 groups. For the unrelaxed

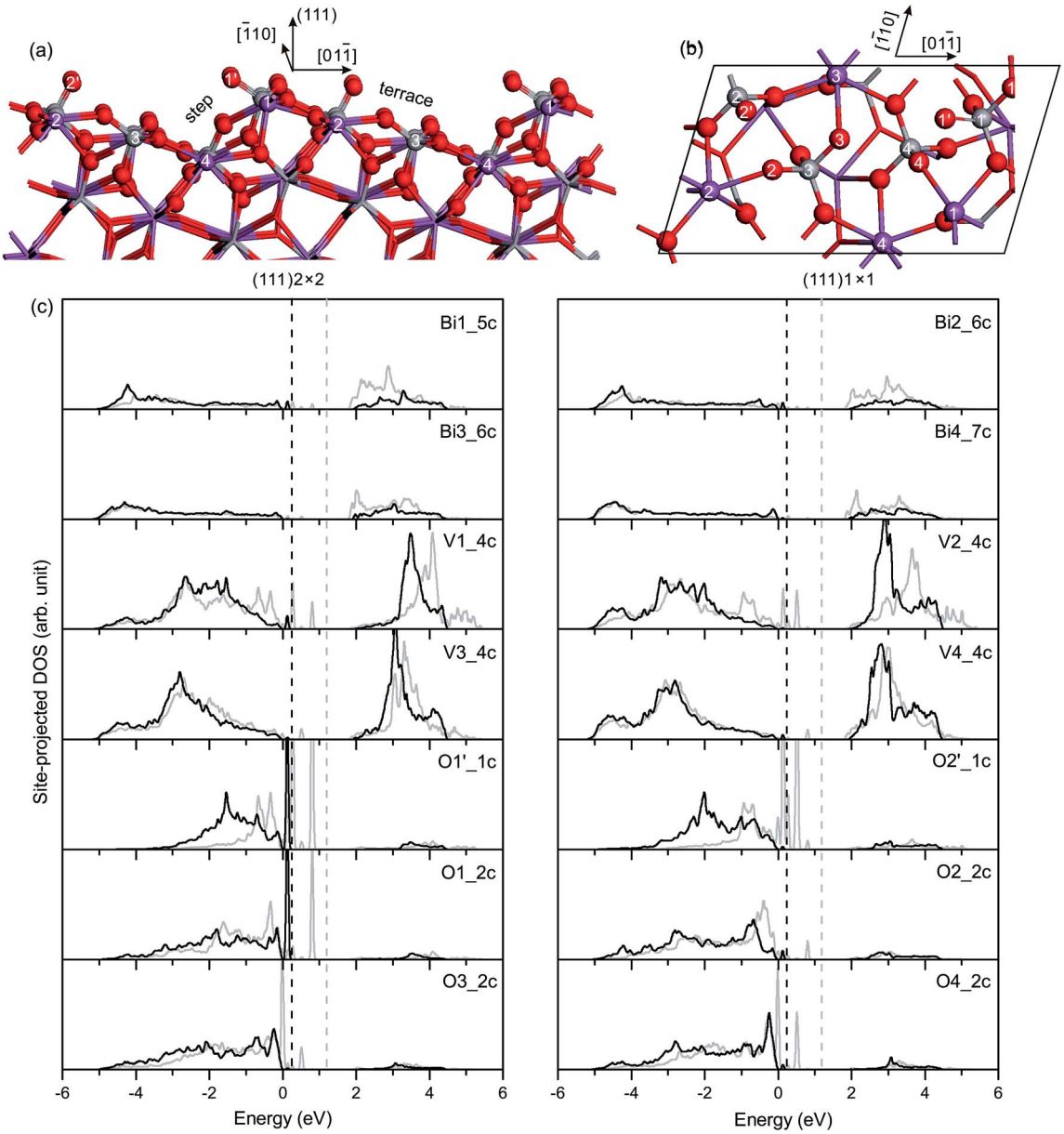

Fig. 7 (a) Side view and (b) top view of the relaxed geometric structure of the fm-$BiVO_4$ (111) surface. (c) Site-projected DOS of specific surface atoms in the relaxed and unrelaxed (111) surface slabs, denoted by black and grey, respectively.

slab, sharp peaks of occupied dangling-bond states lie in the band-gap region. The dangling bonds are derived from the Π_5^8 bonds in the four surface VO_4 groups. Due to surface relaxation, only one peak of the dangling-bond states from the Π_5^8 bonds in the $V1O_4$ group is fixed at 0.1–0.2 eV above the VB top. All other dangling-bond states merge into the bulk VB region. Thus, there are dangling-bond states in the band-gap region of the (111) surface.

3.4 Surface energy and equilibrium morphology

The surface energy σ is defined as

$$\sigma = \lim_{N\to\infty} \left(E_{\text{slab}}{}^{N} - NE_{\text{bulk}}\right) \Big/ 2A, \quad (1)$$

where $E_{\text{slab}}{}^{N}$ is the total energy of a relaxed or unrelaxed N-layer slab and A the area of surface unit cell. Here, we take the computational approach proposed by Fiorentini and Methfessel to obtain relaxed surface energies σ_r of fm-$BiVO_4$.[46] According to this approach, E_{bulk} can be extrapolated by fitting a straight line to $E_{\text{slab}}{}^{N}$ (N = 6, 7, 8, 9, 10), which avoids the so-called "divergence problem" in surface energy calculations. The extrapolated E_{bulk} is then used in eqn (1) to derive accurate relaxed surface energies.

The relaxation energy, *i.e.*, the energy gain due to relaxation of the ideally cut surface, is calculated as $E_{\text{relax}} = (E_{\text{slab}}^{\text{unrelaxed}} - E_{\text{slab}}^{\text{relaxed}})/2A$.[47] Here, $E_{\text{slab}}^{\text{relaxed}}$ and $E_{\text{slab}}^{\text{unrelaxed}}$ denote the total energies of relaxed and unrelaxed slabs, respectively. The unrelaxed surface energy σ_u is then obtained *via* $\sigma_u = \sigma_r + E_{\text{relax}}$.

The calculated unrelaxed surface energies σ_u and relaxation energies E_{relax} for low-index surfaces of fm-$BiVO_4$ can be classified into three groups, as shown in Table 4. The calculated σ_u (E_{relax}) are ~1.7 J m^{-2} (1.1 J m^{-2}) for the (100)/(010) surfaces, 0.46 J m^{-2} (0.15 J m^{-2}) for the (001) surface, and ~1.0 J m^{-2} (0.6 J m^{-2}) for other surfaces. The calculated relaxed surface energies σ_r of fm-$BiVO_4$ indicate a surface stability order of {001} > {011} ~ {101} > {111} > {110} > {010} ~ {100}, in good agreement with reported results.[37] The most stable surface is {001}, in accordance with the fact that fm-$BiVO_4$ exhibits a perfect {001} cleavage.[48]

As is known, the surface energy is associated with the disruption of chemical bonds at the surface. It is therefore reasonable to assume that σ_r is proportional to the density of disrupted chemical bonds at the surfaces with similar geometric structures. Surfaces except (101) and (011) exhibit a good linear relation between σ_r and N_{DB}/A, as shown in Fig. 8. Here, N_{DB} is the number of disrupted Bi–O bonds listed in Table 4. The (101) and (011) surfaces are terminated with only Bi atoms while all other surfaces are terminated with both Bi atoms and VO_4 groups. Thus, the deviation of (101) and (011) from other surfaces can be ascribed to their distinct surface geometric structures.

The equilibrium morphology of a crystal can be determined from the calculated surface energies σ_r *via* Wulff construction.[49] Fig. 9(a) shows an SEM image of fm-$BiVO_4$ samples from our previous work.[24] Fig. 9(b) is the predicted equilibrium morphology of fm-$BiVO_4$, a corner-cut truncated bipyramid with {001}, {101}, {011} and {111} facets exposed. The {101}/{011} facets contribute 77.3%, {001} 22.0%, and {111} 0.7% to the total surface region. The magnified insets demonstrate the good agreement between prediction and measurement. The equilibrium morphology of fm-$BiVO_4$ was widely observed in experiments by others.[23] Compared to the morphology predicted by Zhao *et al.*, our results reveal the existence of {111} facets for real crystals of fm-$BiVO_4$.

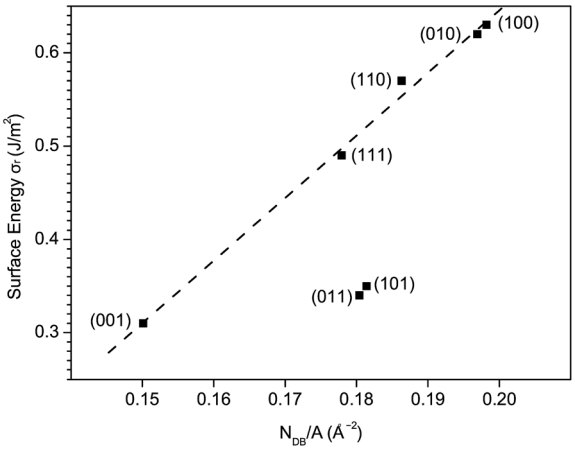

Fig. 8 The relaxed surface energy σ_r *vs.* surface density of disrupted Bi–O bonds N_{DB}/A for low-index surfaces of fm-$BiVO_4$.

3.5 Work function

The work function ϕ is determined by

$$\phi = E_v - E_F, \quad (2)$$

where E_v is the vacuum level and E_F the Fermi level. Here, we take simply the VB edge as E_F for work function calculations since fm-$BiVO_4$ is a semiconductor.[50] There are two contributions to the work function: an intrinsic one due to the binding of electrons and the effect of a dipole layer at the surface.[51] The positive or outward-pointing surface dipole can decrease ϕ.[52]

The calculated surface-dependent work functions of fm-$BiVO_4$ are presented in Table 4. It should be noted that, due to the existence of occupied band-gap states, the E_F of (110) and (111) are 0.2 eV higher in energy than those of other surfaces. Thus, the Fermi level pinning at the surface contributes 0.2 eV to the reduction of the work functions of (110) and (111). Furthermore, the variation in ϕ between the different surfaces of fm-$BiVO_4$ is related to the surface dipole layer. For simplicity, the position of the V atom can be roughly taken as the negative charge center of the VO_4^{3-} anion, and the position of the Bi atom as the positive charge center of the Bi^{3+} cation. As mentioned above, for all unrelaxed surface slabs except (101) and (011), the surface Bi and V atoms are coplanar in the surface plane, indicating that the net surface dipole is approximately zero. However, surface relaxation makes a relative displacement Δd between the surface Bi and V atoms along the surface orientation, inducing a positive surface dipole. The Δd values, proportional to the magnitude of the surface dipole, are 0.08 Å, 0.11 Å, 0.11 Å and 0.19 Å for (001), (110), (111) and (100)/(010), respectively. As is known, the larger the positive surface dipole the smaller the value of ϕ. Therefore, if the Fermi level pinning is not included, ϕ would decrease with increasing Δd in the

Table 4 Area of surface unit cell A in Å^2, number of disrupted Bi–O bonds N_{DB}, relaxed surface energy σ_r, unrelaxed surface energy σ_u and relaxation energy E_{relax} in J m^{-2}, and work function ϕ in eV for low-index surfaces of fm-$BiVO_4$

Surface	{100}	{010}	{001}	{101}	{011}	{110}	{111}
A	60.55	60.93	26.64	33.08	33.25	42.95	89.94
N_{DB}	12	12	4	6	6	8	16
σ_r	0.63	0.62	0.31	0.35	0.34	0.57	0.49
	0.8848 (ref. 37)	—	0.5016 (ref. 37)	0.5517 (ref. 37)	0.5496 (ref. 37)	0.8765 (ref. 37)	—
σ_u	1.67	1.77	0.46	0.92	0.95	1.10	1.02
E_{relax}	1.04	1.15	0.15	0.57	0.61	0.53	0.53
ϕ	6.96	6.90	7.20	5.93	5.98	6.89	6.82

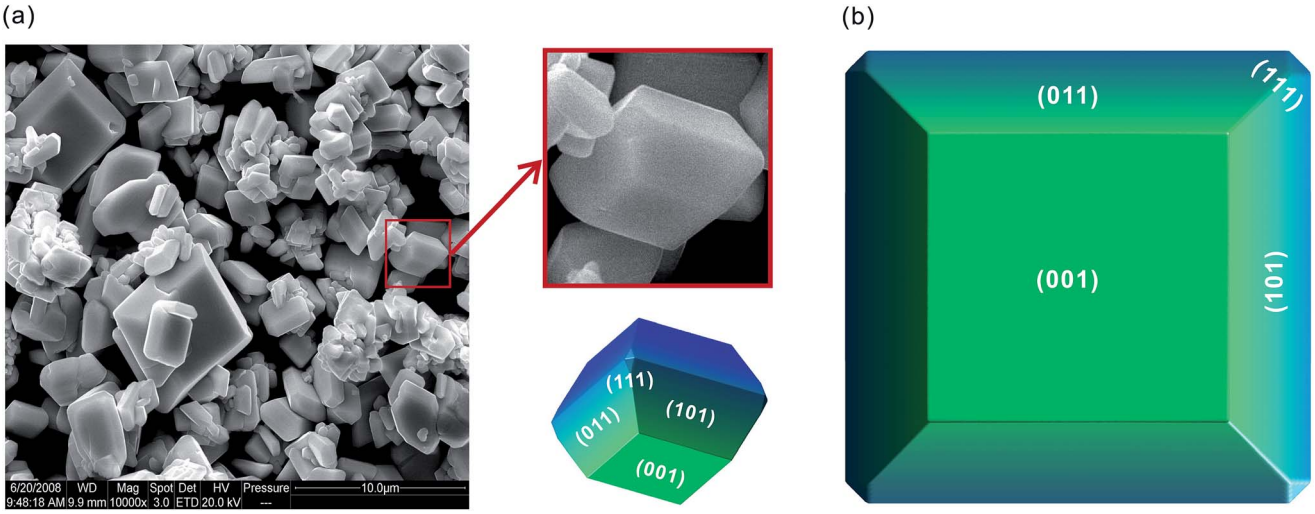

Fig. 9 Equilibrium morphology of fm-$BiVO_4$. (a) The SEM image;[24] (b) prediction.

sequence (001), (110), (111) and (100)/(010). If the Fermi level pinning is included, ϕ would decrease in the sequence (001), (100)/(010), (110) and (111), as shown in Table 4.

For the unrelaxed surface slabs of (101) and (011), the outermost layer is the Bi atom, the sublayer and sub-sublayer are the VO_4 groups, indicating a large outward-pointing permanent surface dipole. Surface relaxation results in a relative displacement Δd of 0.36 Å between the surface Bi and V atoms along the surface orientation. The induced surface dipole is positive, compensating partially for the loss in the permanent surface dipole. In short, the large surface dipole layer remains at the (101) and (011) surfaces, and causes a dramatic reduction of more than 1 eV in the work function.

3.6 Bader charge analysis

The calculated Bader charges on Bi, V and O atoms in bulk fm-$BiVO_4$ are +2.25e, +2.43e and −1.17e, respectively. Here, e denotes the elementary charge. The Bader charge on the Bi atom is close to the assumed +3 oxidation state of the Bi^{3+} cation, indicating that the bonding between Bi and O is mainly ionic in nature. In contrast, the Bader charge on the V atoms is much smaller than the expected +5 oxidation state of the V^{5+} cation, implying that the bonding between V and O is considerably covalent in nature.

In Table 5, we present the calculated Bader charges on all specific surface atoms. Due to the ionic nature of bonding, Bader charges on surface Bi atoms remain around +2.20e. In contrast, Bader charges for all surfaces except (001) are reduced to around +2.0e, −1.0e and −0.7e on the V, twofold-coordinated O and onefold-coordinated O atoms, respectively. The reduction in Bader charges originates from charge transfer between V and O at the surfaces. It is worth noting that the Bader charges on Bi, V and O atoms at the (001) surface are rather close to those in the bulk, indicating that the chemical bonding is almost unchanged in the [001] orientation by surface interruption.

3.7 Oxygen vacancy formation energy

Oxygen vacancies, a common defect in the bulk and at the surface, have a strong impact on functional properties of oxides. In particular, oxygen vacancies are crucial to understanding the surface catalysis of oxides. Here, we use the O-vacancy formation energy E_{vf}^{O} defined as[53]

$$E_{vf}^{O} = E_{tot}^{vac} - E_{tot} + \frac{1}{2}E(O_2), \quad (3)$$

where $E(O_2)$, E_{tot}^{vac} and E_{tot} denote the total energies of molecular oxygen (O_2), vacancy-containing, and vacancy-free oxides, respectively.

The oxygen vacancy in bulk fm-$BiVO_4$ is modelled in a 2 × 2 × 1 supercell. The calculated bulk E_{vf}^{O} is 4.36 eV for both O(1) and O(2). In Table 6 we present the calculated surface E_{vf}^{O} together with the corresponding surface supercells. At the (100)/(010), (110) and (111) surfaces, the onefold-coordinated O1′ atom is most likely to form an oxygen vacancy. The onefold-coordinated O2′ at the (111) surface, however, is rather

Table 5 Bader charges Q(X) in e for X = Bi, V, O at the surfaces of fm-$BiVO_4$

Surface	(100)	(010)	(001)	(101)	(011)	(110)	(111)
Q(Bi_5c)	+2.22	+2.20		+2.19	+2.16	+2.12	+2.16
Q(Bi_6c)			+2.26				+2.09
Q(Bi_6c)							+2.17
Q(Bi_7c)						+2.19	+2.22
Q(V_4c)	+2.03	+2.04	+2.34	+1.99	+2.02	+2.13	+2.01
						+2.05	+1.96
							+1.92
							+1.96
Q(O_1c)						−0.75	−0.79
	−0.70	−0.69					−0.70
Q(O_2c)	−1.10	−1.03	−1.02	−0.97	−0.93	−0.92	−1.03
				−1.03	−1.03	−0.91	−0.92
				−0.99	−1.04		−0.98
							−0.94

Table 6 O-vacancy formation energy E_{vf}^{O} in eV for onefold- and twofold-coordinated O atoms at the surfaces of fm-$BiVO_4$. The size of surface supercell is also presented

Surface	(100)	(010)	(001)	(101)	(011)	(110)	(111)
Size	2 × 1	1 × 2	2 × 2	2 × 2	2 × 2	2 × 2	2 × 1
$E_{vf}^{O\_1c}$	3.38	3.36				3.41	3.40
							3.71
$E_{vf}^{O\_2c}$	3.81	3.76	4.26	4.36	4.33	3.78	3.66
				4.28	4.24	4.46	3.69
				3.80	3.83		3.76
							3.81

stable due to the specific geometry of VO_4 sitting in the terrace of (111). At the (101)/(011) surface, the twofold-coordinated O3 atom in the subsurface VO_4 group tends to form an O vacancy. At the (001) surface, the surface E_{vf}^{O} is 4.26 eV, quite close to the bulk value.

It is interesting to make a comparison of the O-vacancy formation energies between fm-$BiVO_4$ and rutile TiO_2. The calculated E_{vf}^{O} for bulk TiO_2 is 4.11 eV, comparable to that of fm-$BiVO_4$. However, the E_{vf}^{O} at the TiO_2 (110) surface is 2.73 eV, about 0.6–1.5 eV lower in energy than those at the low-index surfaces of fm-$BiVO_4$. As is known, the formation of oxygen vacancies is common at the TiO_2 (110) surface. In contrast, the formation of oxygen vacancies is expected to be rather difficult at the low-index surfaces (especially (001)) of fm-$BiVO_4$. Thus, lattice oxygens are not likely to take part in the oxygen evolution reaction at the surfaces of fm-$BiVO_4$.

4 Discussion

As evidenced by experiments,[25] spatial charge separation occurs between the {001} and the {101}/{011} facets of fm-$BiVO_4$. Photogenerated holes tend to locate at the {101}/{011} facets while photogenerated electrons locate at the {001} facets. A plausible explanation is that the driving force for charge separation is the huge difference of 1.2 eV in work function between {101}/{011} and {001}. As we know, the larger the work function, the lower the Fermi level or band edges. Thus, electrons prefer to locate on the {001} facets ($\phi = 7.20$ eV) while holes prefer to locate on the {101}/{011} facets ($\phi \sim 6$ eV).

There are no band-gap states for all surfaces except (110) and (111), and the band-gap states at the (110) and (111) surfaces are very close to the bulk VB top. Thus, whatever facets are exposed in real crystals, the optical absorption of fm-$BiVO_4$ would remain the same.

It should be kept in mind that the occupied band-gap states act as hole acceptors. When photogenerated holes and electrons migrate to the surfaces, only (110) and (111) could make the photogenerated holes localize at the surface. The localization of holes would reduce the possibility of charge recombination and consequently promote spacial charge separation. As mentioned above, the {111} facets exist in real crystals of fm-$BiVO_4$, although the percentage is small among the exposed facets. If the percentage of {111} or {110} can be enhanced by morphology design, the efficiency of charge separation would be further improved for fm-$BiVO_4$.

Under *in situ* conditions of photocatalytic reactions, the exposed facets of fm-$BiVO_4$ are covered by water and/or cocatalysts. The adsorption of water molecules and/or nanoparticles on the surfaces would modify the intrinsic surface properties of fm-$BiVO_4$, such as the work function and band-gap states. However, to what degree intrinsic surface properties will be modified under *in situ* conditions is still an open question, and deserves further effort.

5 Conclusions

The low-index surfaces of fm-$BiVO_4$ are characterized by surface geometric structures terminated with Bi atoms and VO_4 groups. Similarity in surface geometric structures occurs between (100) and (010) as well as between (101) and (011). There are twofold-coordinated O atoms at the (001), (101) and (011) surfaces, and both onefold- and twofold-coordinated O atoms at the (100), (010), (110) and (111) surfaces. For (101) and (011), surface VO_4 groups are underneath the surface Bi atoms. For all other surfaces except (101) and (011), surface Bi atoms and VO_4 groups are nearly coplanar in the surface plane. At the (100), (010), (110) and (111) surfaces, there are bridge sites for adsorption between neighboring surface Bi atoms.

For the (100), (010), (001), (101) and (011) surfaces, no surface states occur in the band gap region. At the (110) and (111) surfaces, however, there are strongly localized band-gap states derived from the dangling Π_5^8 bonds of surface VO_4 group. The band-gap states are occupied and are located at 0.1–0.2 eV above the bulk VB edge. Surface relaxation has a strong impact on the surface electronic structure for all surfaces except (001). The calculated surface energies of fm-$BiVO_4$ indicate a surface stability order of {001} > {011} ~ {101} > {111} > {110} > {010} ~ {100}. The equilibrium morphology of fm-$BiVO_4$ is predicted as a corner-cut truncated bipyramid with {001}, {101}, {011} and {111} facets exposed, in good agreement with experiments. The percentages of {101}/{011}, {001} and {111} facets are 77.3%, 22.0% and 0.7%, respectively.

The calculated surface-dependent work functions of fm-$BiVO_4$ could be explained through consideration of the surface dipole effect. In particular, the work functions of (101) and (011) are ~6 eV, about 1 eV lower in energy than the work functions of other surfaces. The dramatic difference in work function might provide the driving force for charge separation between {101}/{011} and {001} as observed in the experiment. To further improve the efficiency of charge separation in photocatalysis, the strategy of morphology design could be used to increase the percentage of {111} and (110) facets.

Acknowledgements

This work was financially supported by the National Natural Science Foundation of China (U1404212 and 11404098) and Henan University of Science and Technology (2013ZCX018). G. L. L. thanks W.-X. Li, C. Li, F. Studt, S. Siahrostami, J. K.

Nørskov, D.-P. Sun, W.-C. Ding, D. Wang, and H.-X. Ma for their valuable suggestions and kind help.

References

1 G. Liu, J. C. Yu, G. Q. M. Lu and H.-M. Cheng, *Chem. Commun.*, 2011, **47**, 6763–6783.
2 H. G. Yang, C. H. Sun, S. Z. Qiao, J. Zou, G. Liu, S. C. Smith, H. M. Cheng and G. Q. Lu, *Nature*, 2008, **453**, 638–641.
3 A. L. Linsebigler, G. Lu and J. T. Yates, *Chem. Rev.*, 1995, **95**, 735–758.
4 R. M. Hazen and J. W. E. Mariathasan, *Science*, 1982, **216**, 991–993.
5 L. Hoffart, U. Heider, R. A. Huggins, W. Witschel, R. Jooss and A. Lentz, *Ionics*, 1996, **2**, 34–38.
6 C. Manolikas and S. Amelinckx, *Phys. Status Solidi A*, 1980, **60**, 167–172.
7 A. Tuücks and H. P. Beck, *Dyes Pigm.*, 2007, **72**, 163–177.
8 *High Performance Pigments*, ed. E. B. Faulkner and R. J. Schwartz, Wiley-VCH, Weinheim, 2nd edn, 2009.
9 M. Pasquali and G. Pistoia, *J. Power Sources*, 1989, **27**, 29–34.
10 Y. Zhao, Y. Xie, X. Zhu, S. Yan and S. Wang, *Chem.–Eur. J.*, 2008, **14**, 1601–1606.
11 A. W. Sleight and W. J. Linn, *Ann. N. Y. Acad. Sci.*, 1976, **272**, 22–44.
12 K.-T. Li, M.-Y. Huang and W.-D. Cheng, *Ind. Eng. Chem. Res.*, 1996, **35**, 621–626.
13 A. Kudo, K. Omori and H. Kato, *J. Am. Chem. Soc.*, 1999, **121**, 11459–11467.
14 Y. Liu, B. Huang, Y. Dai, X. Zhang, X. Qin, M. Jiang and M.-H. Whangbo, *Catal. Commun.*, 2009, **11**, 210–213.
15 G. Li, D. Zhang and J. C. Yu, *Chem. Mater.*, 2008, **20**, 3983–3992.
16 H. Hirakawa, S. Shiota, Y. Shiraishi, H. Sakamoto, S. Ichikawa and T. Hirai, *ACS Catal.*, 2016, **6**, 4976–4982.
17 K. Sayama, A. Nomura, Z. Zou, R. Abe, Y. Abe and H. Arakawa, *Chem. Commun.*, 2003, 2908–2909.
18 K. Sayama, A. Nomura, T. Arai, T. Sugita, R. Abe, M. Yanagida, T. Oi, Y. Iwasaki, Y. Abe and H. Sugihara, *J. Phys. Chem. B*, 2006, **110**, 11352–11360.
19 M. D. Hernández-Alonso, F. Fresno, S. Suárez and J. M. Coronado, *Energy Environ. Sci.*, 2009, **2**, 1231–1257.
20 A. W. Sleight, H. y. Chen, A. Ferretti and D. E. Cox, *Mater. Res. Bull.*, 1979, **14**, 1571–1581.
21 G. Xi and J. Ye, *Chem. Commun.*, 2010, **46**, 1893–1895.
22 Y. Sun, C. Wu, R. Long, Y. Cui, S. Zhang and Y. Xie, *Chem. Commun.*, 2009, 4542–4544.
23 X. Meng, L. Zhang, H. Dai, Z. Zhao, R. Zhang and Y. Liu, *Mater. Chem. Phys.*, 2011, **125**, 59–65.
24 D. Wang, H. Jiang, X. Zong, Q. Xu, Y. Ma, G.-L. Li and C. Li, *Chem.–Eur. J.*, 2011, **17**, 1275–1282.
25 J. Zhu, F. Fan, R. Chen, H. An, Z. Feng and C. Li, *Angew. Chem., Int. Ed. Engl.*, 2015, **54**, 9111–9114.
26 M. Oshikiri, M. Boero, J. Ye, Z. Zou and G. Kido, *J. Chem. Phys.*, 2002, **117**, 7313–7318.
27 M. W. Stoltzfus, P. M. Woodward, R. Seshadri, J.-H. Klepeis and B. Bursten, *Inorg. Chem.*, 2007, **46**, 3839–3850.
28 A. Walsh, Y. Yan, M. N. Huda, M. M. Al-Jassim and S.-H. Wei, *Chem. Mater.*, 2009, **21**, 547–551.
29 D. J. Payne, M. D. M. Robinson, R. G. Egdell, A. Walsh, J. McNulty, K. E. Smith and L. F. J. Piper, *Appl. Phys. Lett.*, 2011, **98**, 212110.
30 Z. Zhao, Z. Li and Z. Zou, *Phys. Chem. Chem. Phys.*, 2011, **13**, 4746–4753.
31 Z. Zhao, W. Luo, Z. Li and Z. Zou, *Phys. Lett. A*, 2010, **374**, 4919–4927.
32 M. R. Dolgos, A. M. Paraskos, M. W. Stoltzfus, S. C. Yarnell and P. M. Woodward, *J. Solid State Chem.*, 2009, **182**, 1964–1971.
33 S. Yao, K. Ding and Y. Zhang, *Theor. Chem. Acc.*, 2010, **127**, 751–757.
34 W.-J. Yin, S.-H. Wei, M. M. Al-Jassim, J. Turner and Y. Yan, *Phys. Rev. B: Condens. Matter Mater. Phys.*, 2011, **83**, 155102.
35 M. Oshikiri, M. Boero, A. Matsushita and J. Ye, *J. Electroceram.*, 2009, **22**, 114–119.
36 H. S. Park, K. E. Kweon, H. Ye, E. Paek, G. S. Hwang and A. J. Bard, *J. Phys. Chem. C*, 2011, **115**, 17870–17879.
37 Z. Zhao, Z. Li and Z. Zou, *RSC Adv.*, 2011, **1**, 874–883.
38 http://www.cryst.ehu.es/cryst/get_gen.html.
39 P. E. Blöchl, *Phys. Rev. B: Condens. Matter Mater. Phys.*, 1994, **50**, 17953–17979.
40 G. Kresse and J. Hafner, *Phys. Rev. B: Condens. Matter Mater. Phys.*, 1993, **47**, R558–R561.
41 J. P. Perdew, K. Burke and M. Ernzerhof, *Phys. Rev. Lett.*, 1996, **77**, 3865–3868.
42 S. Maintz, V. L. Deringer, A. L. Tchougréeff and R. Dronskowski, *J. Comput. Chem.*, 2016, **37**, 1030–1035.
43 A. S. Kunju and G. Krishnan, *Group Theory and its Applications in Chemistry*, PHI Learning Pvt. Ltd., New Delhi, 2010.
44 J. W. E. Mariathasana, R. M. Hazenb and L. W. Finger, *Phase Transform.*, 1986, **6**, 165–174.
45 I. Ivanov and J. Pollmann, *Phys. Rev. B: Condens. Matter Mater. Phys.*, 1981, **24**, 7275–7296.
46 V. Fiorentini and M. Methfessel, *J. Phys.: Condens. Matter*, 1996, **8**, 6525–6529.
47 N. V. Skorodumova, M. Baudin and K. Hermansson, *Phys. Rev. B: Condens. Matter Mater. Phys.*, 2004, **69**, 075401.
48 O. v. Knorring, T. G. Sahama, M. Lehtinen, P. Rehtijärvi and J. Siivola, *Contrib. Mineral. Petrol.*, 1973, **41**, 325–331.
49 M. A. Lovette, A. R. Browning, D. W. Griffin, J. P. Sizemore, R. C. Snyder and M. F. Doherty, *Ind. Eng. Chem. Res.*, 2008, **47**, 9812–9833.
50 W. Liu, W. T. Zheng and Q. Jiang, *Phys. Rev. B: Condens. Matter Mater. Phys.*, 2007, **75**, 235322.
51 A. Groß, *Theoretical Surface Science: A Microscopic Perspective*, Springer-Verlag, Berlin, 2nd edn, 2009.
52 T. C. Leung, C. L. Kao, W. S. Su, Y. J. Feng and C. T. Chan, *Phys. Rev. B: Condens. Matter Mater. Phys.*, 2003, **68**, 195408.
53 M. V. Ganduglia-Pirovano, A. Hofmann and J. Sauer, *Surf. Sci. Rep.*, 2007, **62**, 219–270.

